Chapter 4
A Technique for Determining True Deformation Diagrams Under Dynamic Tension Using DIC

Artem V. Basalin, Anatoly M. Bragov, Aleksandr Yu. Konstantinov,
and Andrey R. Filippov

Abstract This article describes a pneumodynamic experimental setup created in the laboratory of dynamic tests of the Research Institute of Mechanics of the Nizhny Novgorod State University and designed to study the dynamic behavior of structural materials at average strain rates of the order of 10-100 s^{-1}. Modern means of registration of parameters of dynamic processes are applied. The results of approbation are given on the example of dynamic tests of samples of sheet steel 09G2S. The technical and true strain diagrams in the static and dynamic range of strain rates are determined.

Key words: Strain rate · Experimental study · Plastic strain · Yield strength · DIC · Experiment · Strain rate

4.1 Introduction

Interest in the study of dynamic deformation and fracture of materials is due to the fact that a large number of important problems in assessing the strength of new critical structures requires specifying the strength and deformation characteristics of materials as functions of the strain rate. Such dependences are extremely important for obtaining reliable estimates of the stress-strain state and strength of structures experiencing dynamic loads as a result of technological accidents, terrorist attacks, falls, etc. To determine the characteristics of materials at high deformation rates, the Hopkinson split bar method [1] and its modifications are often used [2]-[10].

Artem V. Basalin · Anatoly M. Bragov · Aleksandr Yu. Konstantinov · Andrey R. Filippov
National Research Lobachevsky State University of Nizhny Novgorod, 23 Gagarin Avenue, Nizhny Novgorod 603022, Russian Federation,
e-mail: artem.basalin@mech.unn.ru, bragov@mech.unn.ru, konstantinov@mech.unn.ru, filippov@mech.unn.ru

H. Altenbach et al. (eds.), *Sixty Shades of Generalized Continua*,
Advanced Structured Materials 170, https://doi.org/10.1007/978-3-031-26186-2_4

The range of deformation rates from 10^0 s^{-1} to 10^2 s^{-1} is currently poorly understood, but this range of deformation rates is critically important for assessing the strength of structures during a fall and low-speed impact. There are a number of works devoted to the study of the behavior of structural materials in the range of average deformation rates. In [11], the influence of the deformation rate on the mechanical properties during stretching of the industrial aluminum alloy AA7081 was analyzed. Tests at medium strain rate were carried out on a hydropneumatic machine (HPM) [12]. The method of conducting the test is described in detail in [13]-[15]. The deformation rate obtained with this installation was about 30 s^{-1}.

To study the strength and deformation characteristics of sandstone, stress-strain relationships were obtained under uniaxial compression at strain rates of $10^{-2} \sim 55$ s^{-1} using MTS and the drop weight test in [16]. Groth et al. [17], Zhang and Zhao [18], as well as Ma et al. [2, 20] performed low-speed and high-speed impact tests of rocks in the deformation velocity ranges of $10^{-5} \sim 10^{-2}$ s^{-1} and $10^1 \sim 10^2$ s^{-1} using a hydraulic testing machine and an RSG installation with larger bars diameter. One of the difficulties of testing at moderate strain rates is the short duration of the load pulse. Thus, for a limited time of loading at a low speed, it is not possible to achieve significant deformations of the sample. This problem is partially solved in schemes with a prestressed loading elastic bar. The duration of the load in this case turns out to be significant. In [21, 22] the effects of strain rate, temperature, and size effects of three steels used in the nuclear industry were studied at the facility. In [23], the study of the behavior of steels Armox 500T and Armox 600T was carried out in the range of strain rates 100-1000 s^{-1}. A single bar tensile Hopkinson apparatus was used. The tensile force was generated with pendulum. Zabotkin et al. [24] showed the design concept of an instrumented falling weight impact (IFWI) tester and tested 316L stainless steel, titanium alloy, and alloy C22 under medium strain rates.

In [25] an investigation into the effect that medium strain rates have on the mechanical properties of cold drawn mild steel and 304L stainless steel was carried out using two 6 mm diameter by 14 mm long specimens machined from each grade of steel. The tests were performed using an Instron test machine under a quasi-static strain rate, and a high capacity instrumented falling weight axial impact (IFWI) test rig developed at the University of Wollongong was used to con-duct the medium strain rate tests.

In [26] high-speed tensile tests were performed on a Zwick/Roell HTM5020 high-speed testing system (Ulm, Germany) with a maximum test velocity of 20 m/s, as well as a maximum load of 50 kN. The mechanical properties and failure behavior of long glass fiber reinforced thermoplastic composites were investigated. The dynamic tensile tests were carried out at the strain rates of 1, 10, 100, 200, and 400 s^{-1}.

Determination of the true deformation diagrams of materials from static and dynamic stretching experiments is complicated by the process of localization of deformation (neck formation), which violates the uniformity of the VAT and leads to a local change in the distribution of deformations and the type of stress state, which makes it impossible to directly determine stresses and deformations in the sample based on integral displacements and forces, which are measured in the experiment. In a dynamic experiment, the localization of deformations also affects the history of changes in the deformation rate, which increases sharply in the neck region. These features of the interpretation of the results of the dynamic experiment are considered in [27, 28]. In this case, correction of the deformation curve beyond the point of localization of deformation is required [29].

Various methods have been proposed to evaluate effective von Mises stresses in a tensile experiment [30]-[38]. In [39], the DIC system was used to obtain deformation fields. It has been proved that this method is an effective method for registering the deformation of composites [40]-[44]. The article describes a pneumodynamic experimental setup created in the dynamic testing laboratory of the Nizhny Novgorod State University Mechanics Research Institute to study the dynamic behavior of structural materials at deformation rates of the order of 100 s^{-1}. The technique of obtaining true deformation diagrams using DIC is also considered.

4.2 Pneumatic Dynamic Installation for Testing Materials at a Deformation Rate of the Order of 10-100 s^{-1}

Currently, there is a need to develop and implement an experimental scheme and methodology that allows achieving the specified strain rates. This paper describes the unique pneumatic dynamic installation created for testing materials at a deformation rate of the order of $10 - 10^2$ s^{-1}. The scheme of installation and obtaining information used to determine the mechanical characteristics of materials and their dependences on the deformation rate is described.

4.2.1 Installation Scheme

The general scheme of the experimental installation is shown in Fig. 4.1. The sample dimensions are shown in the Fig. 4.2. The compressor 1 is used to create high pressure in the chamber 2. The pressure value is controlled using a pressure gauge 3. The pressure from the cylinder can be directed either to the lower or upper part of the pneumatic cylinder using a distributor 6. Depending on this, it is possible to ensure the movement of the rod either up or down. The stroke of the cylinder rod is 600 mm. The diameter of the hydraulic cylinder piston is 200 mm. The maximum pressure for which the distributor is designed is 10 bar. The magnitude of the applied force is controlled by the pressure in the cylinder chambers. The maximum force generated by the pneumatic cylinder is 31 kN. The upper part of sample 9 is rigidly fixed in the installation frame. The lower part is connected to a movable rod. The upper blade part of the sample (right part on the figure) is longer than the lower one for installation of the strain gauges.

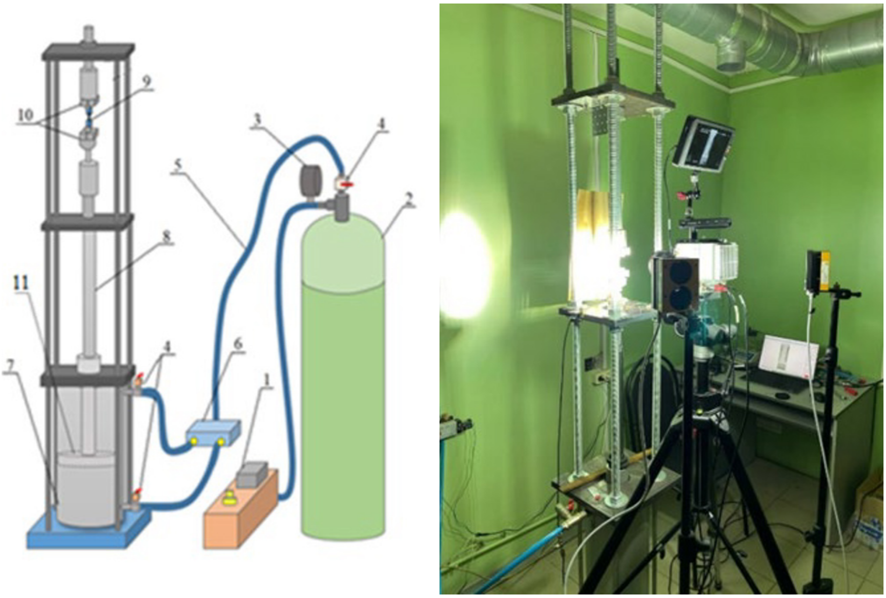

Fig. 4.1: Experimental installation: 1 - compressor, 2 – high pressure chamber, 3 - pressure gauge, 4 - ball valves, 5 - connecting hoses, 6 - solenoid valves, 7 - pneumatic cylinder, 8 - lower movable bar, 9 - sample, 10 - grips, 11 - the piston.

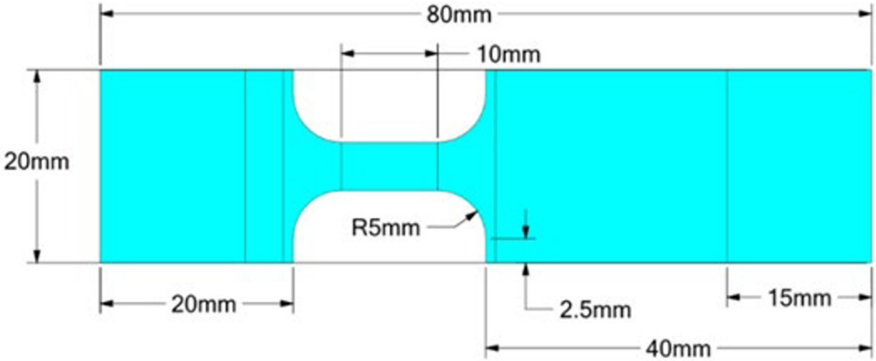

Fig. 4.2: Sample dimension.

4.2.2 Methods of Obtaining and Processing Information in the Experiment

In the laboratory of the Research Institute of Mechanics of the UNN has a licensed VIC-2D non-contact measurement of deformation fields by Correlated Solutions, which includes a high-speed Phantom VEO 710 L camera with high resolution for video recording of the deformation process of a sample during dynamic tests (compression, stretching, shear, three- or a four-point bend), a powerful LED illuminator, a computer with specialized DIC (digital image correlation or digital image correlation method) software installed, and a number of additional devices and devices: a tripod for the camera, stands for illuminators, a device for applying speckles to samples.

The preparatory stage consists in the preliminary application to the surface of the test sample of a contrasting finely dispersed spray, which is a collection of randomly located black dots on a white matte base, the so-called speckle structure, Fig. 4.3 (left). The object under examination is illuminated by a LED monochrome uniform illumination system, which illuminates the outer edges and the central part of the inspection surface with equal intensity, which significantly improves the quality of the measurement results. Next, the camera records images of the investigated object surface corresponding to different phases of the object deformation process. Changes in the position of points of an inhomogeneous surface structure are processed by special high-precision correlation algorithms. The location of points for further analysis of the deformation processes of the samples is shown to the right (Fig. 4.3). The deformation of the sample was observed in two cases.

The average deformation of the working part was determined by the displacements of the reference points P0 and P1 according to the formula:

$$\varepsilon_{\text{avg}} = \ln\left(\frac{L_{\text{P1}-\text{P0}}}{L^{0}_{\text{P1}-\text{P0}}}\right) \tag{4.1}$$

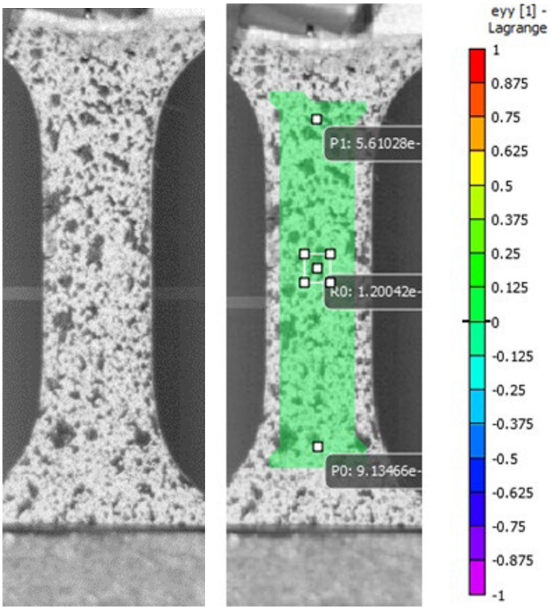

Fig. 4.3 Surface of the test sample: speckle structure (left), location of points for further analysis of the deformation processes (right).

where L_{P1-P0} is the distance between points P1 and P0 at the current time, L^0_{P1-P0} - distance between points P1 and P0 at time 0. The local deformation was determined by averaging the effective von Mises deformations calculated by the DIC method over a small region R0 in the zone of deformation localization.

The strain rates were determined by differentiating the time dependences of the strains. The loading rate was varied by changing the pressure in the working chamber of the installation. Tests were carried out with pressures of 2, 4 and 6 atm in a high pressure chamber. The results of the analysis of the processes of dynamic deformation of the samples are shown in the figure. Figure 4.4a) shows the time dependences of local deformations, Fig. 4.4b) shows the strain rates.

Figures 4.5 and 4.6 show the results of comparing the time histories of average and local strains (a) and strain rates (b) for two loading modes. It can be seen that up to a certain moment (localization time 15 ms), the average and local values are

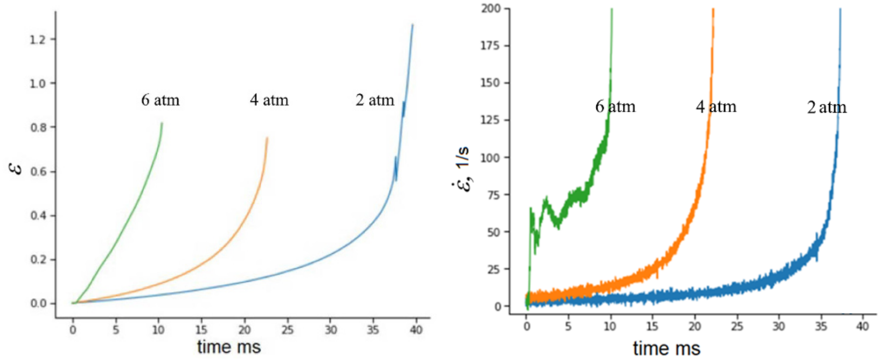

(a) (b)

Fig. 4.4: Results of the analysis of the processes of dynamic deformation: time dependences of local deformations (a), strain rates (b).

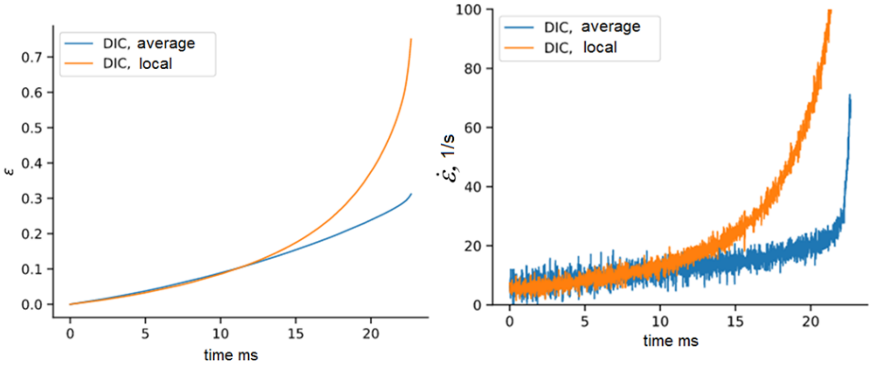

(a) (b)

Fig. 4.5: Time histories of average and local strains (a) and strain rates (b).

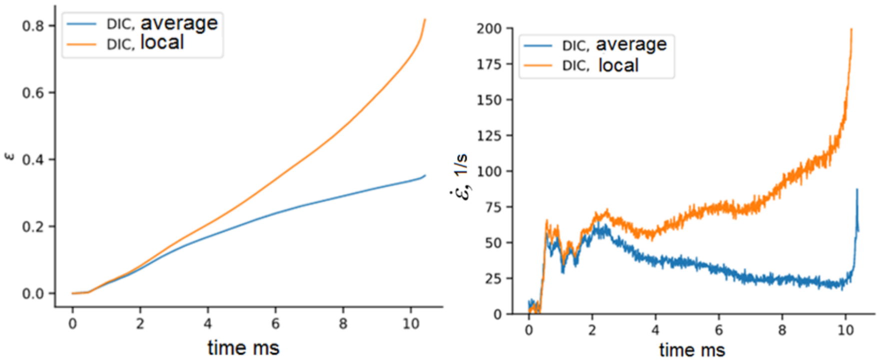

(a) (b)

Fig. 4.6: Time histories of average and local strains (a) and strain rates (b).

in good agreement. Up to this point in time, the values of stresses and strains are distributed uniformly along the length of the sample. Later, a neck is formed in the sample.

Figure 4.7 illustrates the strain fields (strains along the vertical axis) at different time points. One can see the localization of deformation (2 ms) in the middle part of the sample. The right side of Figs. 4.8 and 4.9 shows graphs characterizing the distribution of axial deformation of the sample at different points in time. The line on which these distributions were built is illustrated on the left side of Figs. 4.8 and 4.9. The coordinates of the points on the line are plotted along the horizontal axis, and the deformation values are plotted along the vertical axis. One can observe the process of deformation localization.

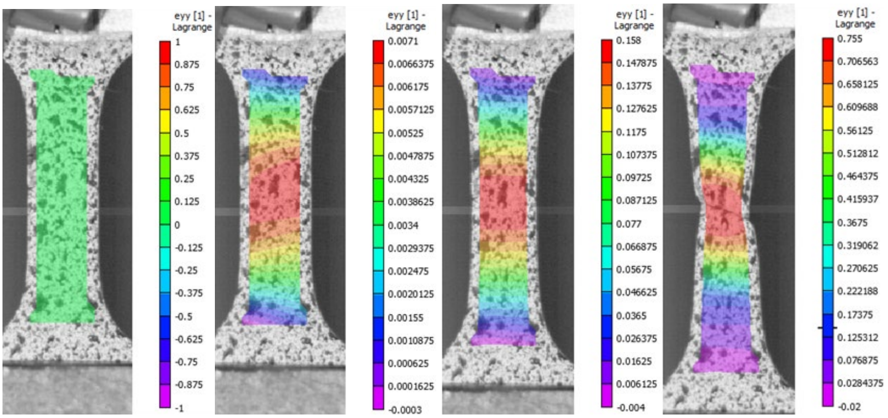

Fig. 4.7: Strain fields (strains along the vertical axis) at different times.

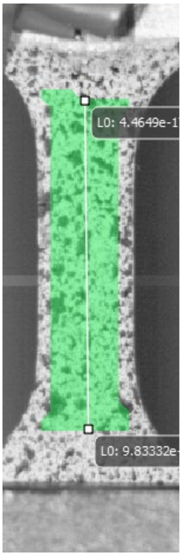

Fig. 4.8 Distribution of axial deformation: location of the strains.

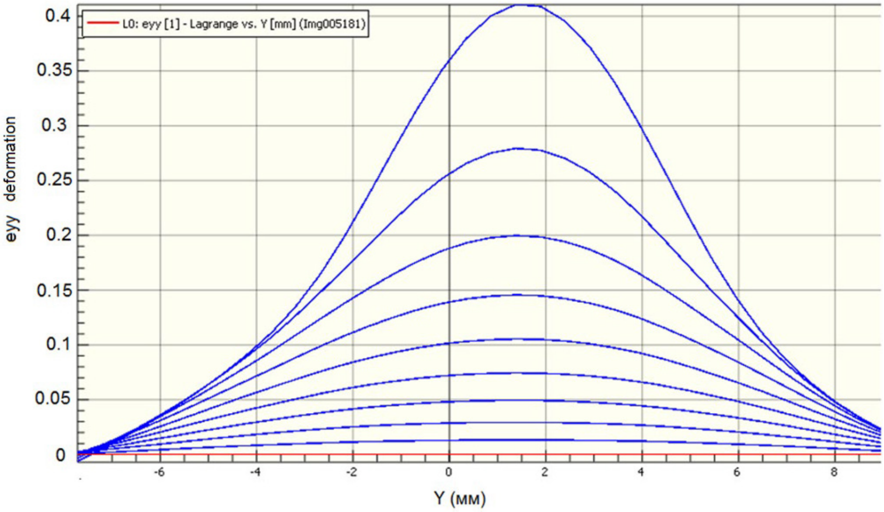

Fig. 4.9: Distribution of axial deformation: strains vs. coordinates of the points of the line.

To register the forces acting on the sample during loading, strain gauges were glued to the blade part of the sample. The experimental circuit uses a potentiometric circuit for connecting strain gauges. Calibration of the measuring channel is carried out by the electrical method. The oscilloscope allows you to record electrical voltages in the power supply circuit of sensors. Strain gauge deformation is associated with a change in its resistance by the main strain gauge dependence:

$$k\varepsilon = \frac{\Delta R}{R},$$

where k is the strain gauge sensitivity coefficient, ε is the strain gauge deformation, ΔR is the change in strain gauge resistance and R is the initial strain gauge resistance.

The calibration procedure is used to determine the conversion factor of the voltage registered by the oscilloscope into the strain gauge deformation. For this, a known resistance R_c is periodically switched on in the strain gauge power supply circuit using a relay. Thus, the change in the resistance of the strain gauge by the value of Rc is modeled. With the help of an oscilloscope, the corresponding change in the electrical voltage in the sensor supply circuit ΔU_c is recorded.

Since the voltage jump is proportional to the change in the resistance of the circuit, you can make the following proportion:

$$\frac{\Delta U_c}{R_c} = \frac{\Delta U}{\Delta R},$$

where ΔU_c is the voltage jump during the calibration procedure, R_c is the additional resistance, ΔU is the voltage jump during experiment and ΔR is the change of strain gauge resistance during experiment.

From the above formulas it follows:

$$\varepsilon = \frac{R_c}{k\Delta U_c R}\Delta U$$

Thus, the conversion coefficient (calibration coefficient) is equal to:

$$K = \frac{R_c}{k\Delta U_c R}.$$

It has the dimension of [1/V].

The signal recorded with the help of strain gauges glued on the blade part of the sample is shown in Fig. 4.10.

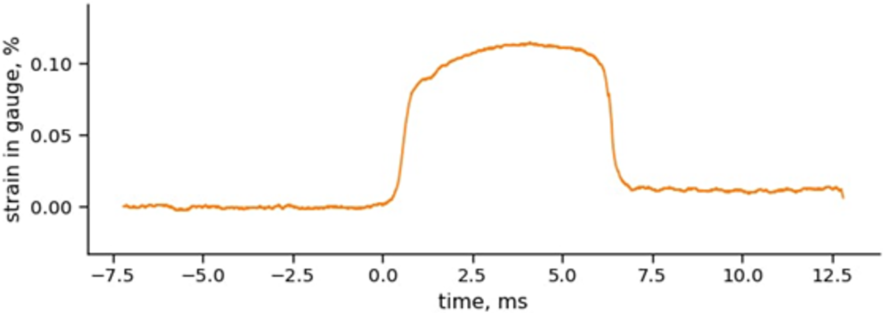

Fig. 4.10: Strains in gauge vs. time.

The force that acts on the sample during loading is calculated as follows:

$$F(t) = \varepsilon_{\mathrm{e}}(t) E w_{\mathrm{g}} h_{\mathrm{g}} \tag{4.2}$$

where $\varepsilon_{\mathrm{e}}(t)$ - is the elastic deformation of a certain section of the blade part of the sample, E - is the Young's modulus of the sample material, $A_{\mathrm{g}} = w_{\mathrm{g}} h_{\mathrm{g}}$ - is the sectional area of the sample in the blade part at the location of the strain gauges, w_{g} and h_{g} are the width and thickness of the blade parts of the sample, respectively. The technical stress is determined by dividing the magnitude of the force by the initial cross-sectional area of the sample:

$$\sigma_{\mathrm{tech}}(t) = \frac{F(t)}{w_0 h_0} \tag{4.3}$$

Excluding time as a parameter from the dependences $\varepsilon(t)$ and $\sigma(t)$, we obtain the strain curve $\sigma(\varepsilon)$ with the known law of change in the strain rate $\dot{\varepsilon}(\varepsilon)$ during loading of the sample. To determine the true stress at any given time, using high-speed recording data, the force acting on the sample is divided by the current area of the minimum section of the sample. Determining the width of the sample based on the results of video recording is carried out automatically using machine vision tools. The process of tracking the position of reference points is shown in Fig. 4.11. Figure 4.12 illustrates the time dependence of the width of the working part of the sample.

It is assumed that the thinning of the sample in the direction normal to the plane of the plate is proportional to the change in the width of the working part. Then the true voltage at each moment of time can be calculated by the formula:

$$\sigma_{\mathrm{true}}(t) = \frac{F(t)}{w(t)h(t)} = \frac{F(t)}{w^2(t)\frac{h_0}{w_0}} \tag{4.4}$$

where $w(t)$ - is the width of the working part of the sample at time t, $h(t)$ - is the thickness of the working part of the sample at time t, w_0 and h_0 - are the initial values of the width and thickness of the working part of the sample. Figure 4.13 compares the time dependences of the technical and true stress in the specimen, and Fig. 4.14 illustrates the comparison of the technical and true stress-strain diagrams.

The performed debugging tests allow us to conclude that the DIC method provides comprehensive information about the process of dynamic deformation of the sample. The resolution of the high-speed camera both in space and time is sufficient to determine the required characteristics of the process.

4.3 Test Results of Sheet (3 mm) Steel 09G2S in a Wide Range of Strain Rates

Steel 09G2S belongs to the class of structural low-alloy steels. This material is used for the manufacture of various parts and elements of welded metal structures

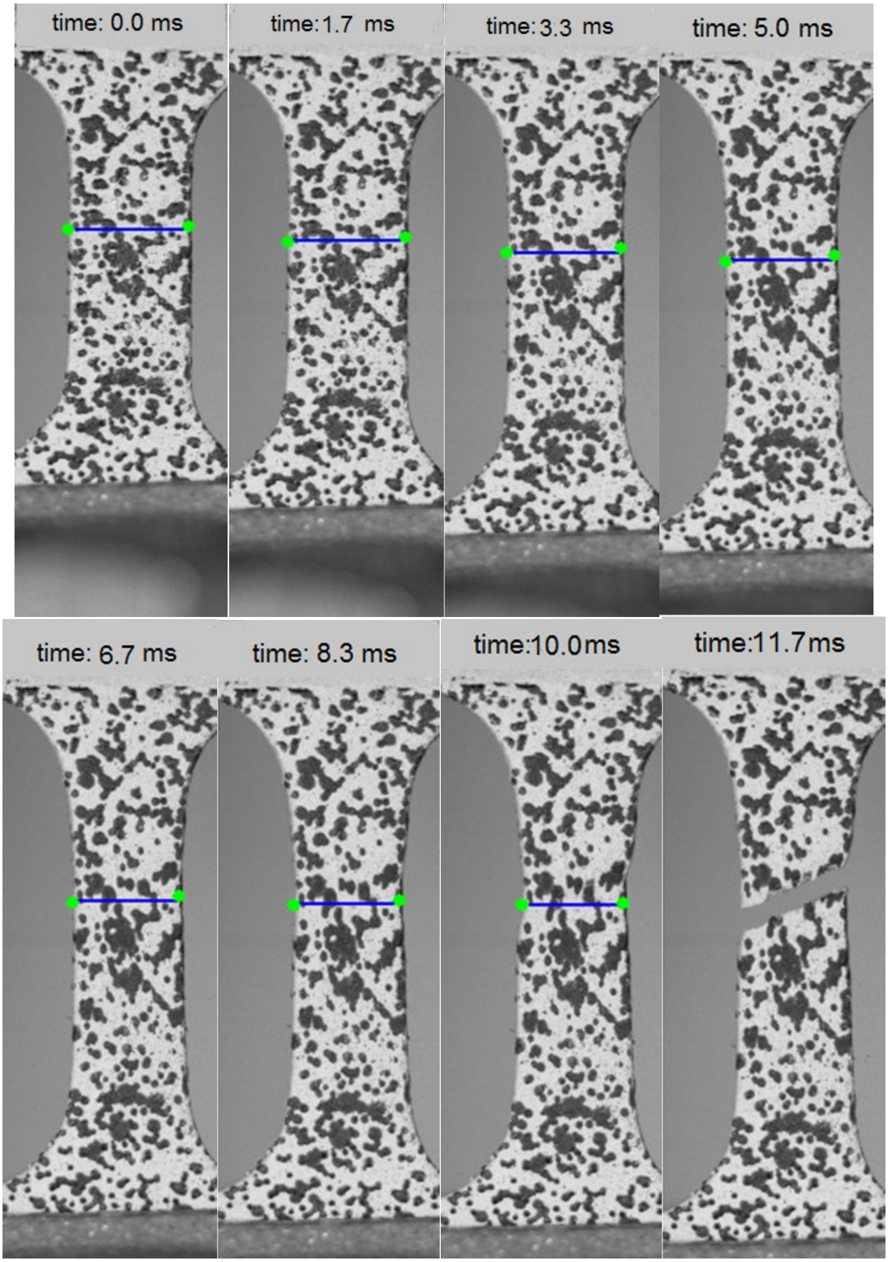

Fig. 4.11: Process of tracking the position of reference points.

Fig. 4.12 Time of the width of the working part of the sample.

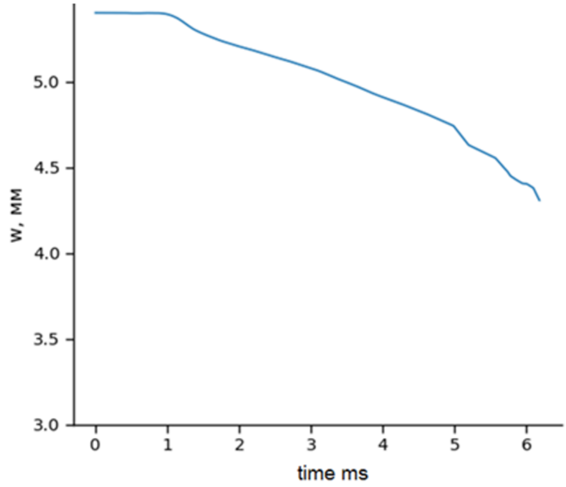

Fig. 4.13 Time vs. technical and true stress.

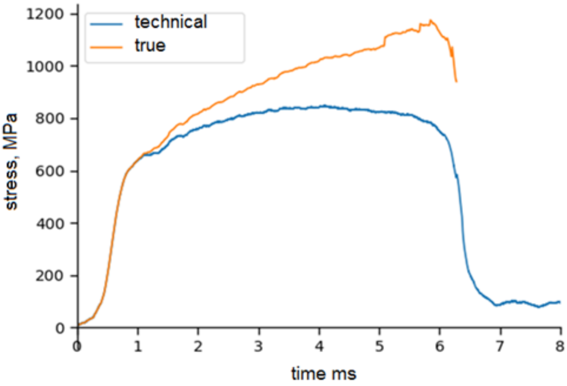

Fig. 4.14 Technical and true stress-strain diagrams.

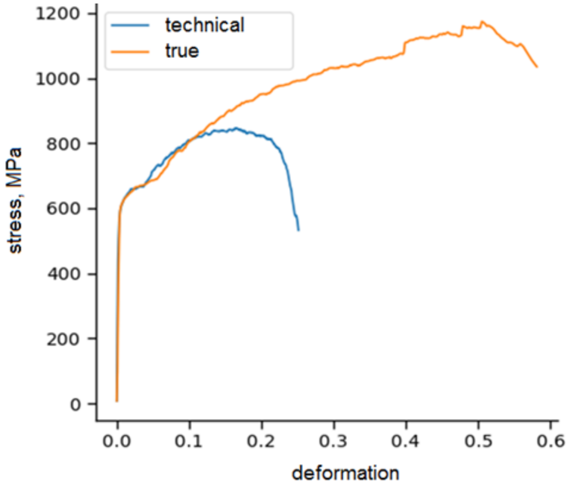

operating at temperatures from -70 to 425° C under pressure. The high strength of the material and good indicators of deformation properties in a wide temperature range, the ability to change the properties of the alloy after heat treatment, a wide choice of different grades, a variety of thicknesses have led to the wide use of this alloy in many areas of production and engineering.

Building structures, pipes for transporting various liquids (water, oil, etc.) and gases, tanks for various purposes, steam boilers, oilfield equipment and various machine parts, including agricultural ones, are made from 09G2S steel. Of interest are the rate dependences of the mechanical characteristics of this alloy for predicting the behavior of structures made of this material under shock loads. In this section, for the first time, the results of studying the deformation and fracture of specimens from the 09G2S alloy in a wide range of deformation rates are presented.

The test specimens were made from a 3 mm thick sheet. Static tensile tests were carried out on the Z100 ZWICK-ROEL test facility. High-speed tests (with strain rates above 500 1/s) under compression and tension were carried out on a setup that implements the Kolsky method. The tests were carried out on high-strength steel measuring bars with a diameter of 20 mm. Tensile tests with intermediate strain rates (of the order of 100 1/s) were carried out on a pneumodynamic experimental setup created in the course of the dissertation research.

For static tests, samples with a working part width of 20 mm, a thickness of 3 mm, and a working part length of 120 mm were used. The tests were carried out until the destruction of the sample. The view of the sample after testing is shown in Fig. 4.15. Figure 4.16 illustrates the technical deformation curves determined during stat-ic tests of specimens made of steel 09G2S. It can be seen from the presented diagram that the deformation diagram has a yield point (A-B).

To build a true strain curve, the section of the diagram located to the right of the strain localization point (the point of maximum stress on the technical strain diagram) was discarded. For the point corresponding to the fracture moment of the sample, plastic deformation and average stress were determined as follows:

$$\varepsilon_{\mathrm{f}} = \ln\left(\frac{1}{1-\psi}\right), \tag{4.5}$$

$$\sigma_{\mathrm{f}} = \frac{\sigma_{\mathrm{y}}}{1-\psi} \tag{4.6}$$

where ψ is the relative constriction at rupture, σ_{y} is the conditional (technical) stress at which the rupture occurred.

The true deformation curves of steel 09G2S are shown in Fig. 4.17. The dotted

Fig. 4.15: Sample after testing.

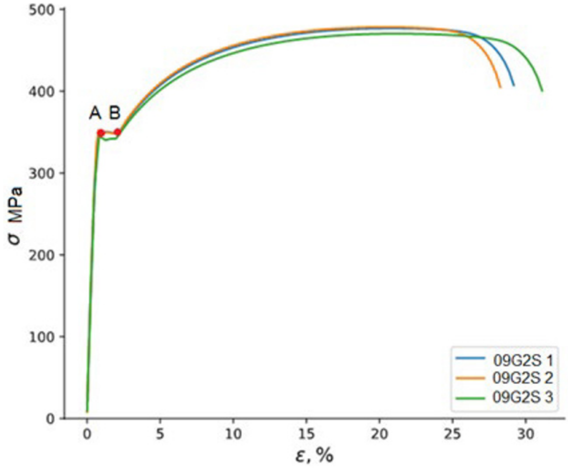

Fig. 4.16 Engineering stress-strain diagrams.

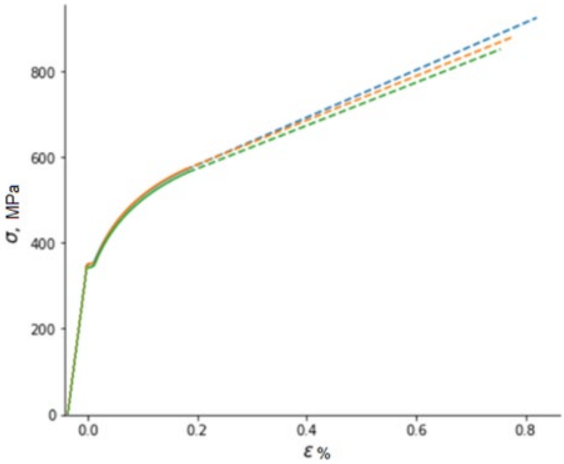

Fig. 4.17 True stress-strain diagrams.

line shows the section of the linear approximation of the diagram, connecting the point of the beginning of the localization of deformation and the point of rupture of the sample. High-speed tensile tests were carried out using a modification of the Kolsky direct tensile method.

To determine strain diagrams in tension at a strain rate of about 100 1/s, the previously described pneumodynamic setup was used. Samples-plates with a working part length of 10 mm, a working part width of 5.4 mm, and a thickness of 0.7 mm were tested. The test results are shown in Fig. 4.18. The dotted line shows the history of change in the strain rate of the samples during loading (right vertical axis). It can be seen that a deformation rate close to a constant value is realized. Figure 4.19 shows the results of static and dynamic tests.

The dependence of the initial tensile yield strength on the strain rate is shown in Fig. 4.20. The rate dependences of the ultimate fracture characteristics of steel 09G2S

Fig. 4.18 True stress-strain and stress-strain rate diagrams.

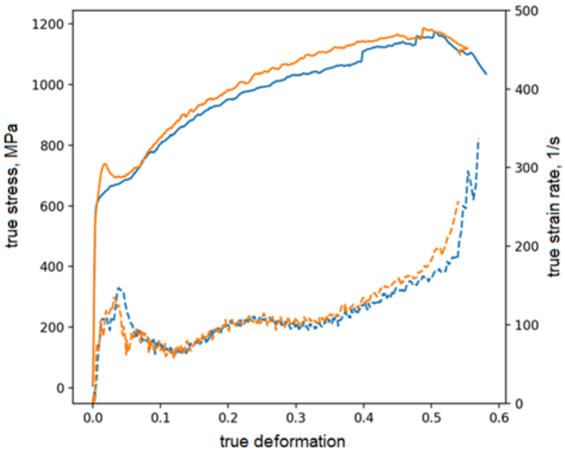

Fig. 4.19 True stress-strain diagrams.

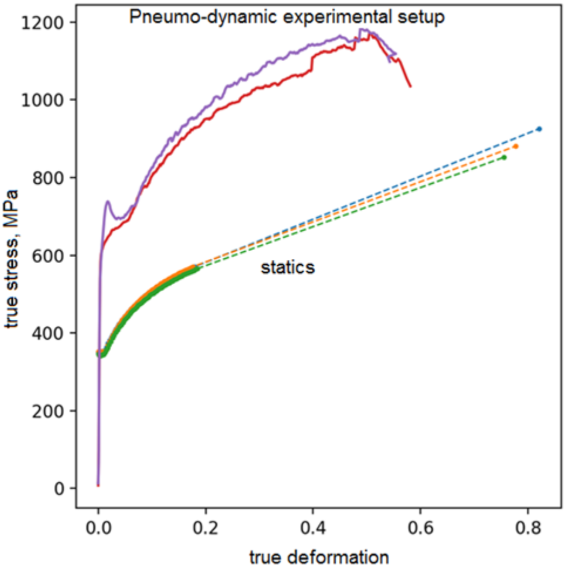

are shown in Fig. 4.21 (ψ relative narrowing after rupture, δ relative elongation after rupture). Blue stars represent static test data, red round markers - data obtained on a pneumodynamic installation, orange squares - results of testing samples with a base of 8 mm on the split Hopkinson bar, green triangles - results of testing samples with a base of 5 mm on the split Hopkinson bar. It can be seen that the ultimate elongation after rupture (left side of the figure) strongly depends on the sample base. The limiting narrowing, which characterizes the plastic deformation of fracture under conditions of pronounced localization of deformation, is practically independent of the strain rate.

Fig. 4.20 Initial tensile yield strength vs. strain rate.

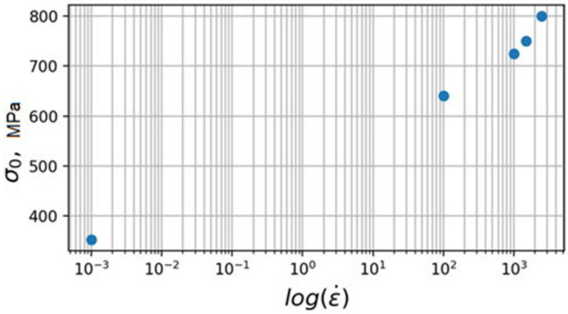

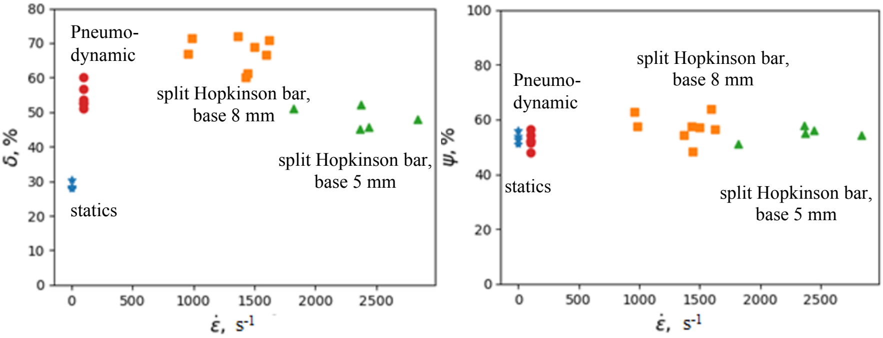

Fig. 4.21: Ultimate fracture characteristics of steel 09G2S.

The scatter of the limiting values δ is significantly higher for the limiting value of the narrowing ψ. In this regard, ψ is most often used in the strain-type failure criteria.

4.4 Conclusion

1. The experimental setup described in the paper makes it possible to study the processes of deformation and destruction of lamellar specimens at moderate strain rates.
2. To improve the accuracy of measuring the strains of the working part of the sample, high-speed video registration was used in combination with the DIC tool.
3. The DIC method was used to construct true strain diagrams taking into account the heterogeneity of strain fields in the working part of the specimen.
4. The results of testing specimens of steel 09G2S in a wide range of strain rates are presented, showing a significant effect of strain rate on the yield strength of the studied material. The limiting characteristics of plasticity in this case are practically independent of the strain rate.

Acknowledgements The work was supported by the Russian Science Foundation grant no. 21-19-00283.

References

[1] Hopkinson B (1914) A method of measuring the pressure produced in the detonation of high explosives or by the impact of bullets, Philosophical Transactions of the Royal Society of London, Series A Containing Papers of a Mathematical or Physical Character **213**:437–456. DOI 10.1098/rsta.1914.0010

[2] (Rusty) Gray GT III (2000) Classic Split-Hopkinson Pressure Bar Testing, In: Mechanical Testing and Evaluation, Vol 8, ASM Handbook (Kuhn H, Medlin D Eds), ASM Int, Materials Park OH, pp 462–476. DOI 10.31399/asm.hb.v08.a0003296

[3] Bragov AM, Lomunov AK (1984) Features of the construction of strain diagrams by the Kolsky method (in Russ), Applied Problems of Strength and Plasticity **28**:125-137.

[4] Caverzan A, Cadoni E, di Prisco M (2012) Tensile behaviour of high performance fibre-reinforced cementitious composites at high strain rates, International Journal of Impact Engineering **45**:28-38. DOI 10.1016/j.ijimpeng.2012.01.006

[5] Davies RM (1948) A critical study of the Hopkinson pressure bar, Philosophical Transactions of the Royal Society of London, Series A **240**:375–457. DOI 10.1098/rsta.1948.0001

[6] Eskandari H, Nemes JA (2000) Dynamic testing of composite laminates with a tensile split Hopkinson bar, Journal of Composite Materials **34**(4):260-273. DOI 10.1177/002199830003400401

[7] Gama BA, Lopatnikov SL, Gillespie JW Jr (2004) Hopkinson bar experimental technique: A critical review. Applied Mechanics Reviews **57**4:223-250. DOI 10.1115/1.1704626

[8] Jiang B, Zhang R (2006) Tensile properties in the through-thickness direction for a carbon fiber woven reinforced composite at impact loading rate, Journal de Physique IV **134**(1):1071–1075. DOI 10.1051/jp4:2006134164

[9] Kolsky H (1949) An investigation of the mechanical proper-ties of materials at very high rates of loading, Proceedings of the Physical Society, Section B, **62**(11):676–700. DOI 10.1088/0370-1301/62/11/302

[10] Lomunov AK (1987) Methodology for studying the processes of viscoplastic deformation and material properties based on the split Hopkinson bar (in Russ), PhD thesis, 1987.

[11] Cadoni E, Dotta M, Forni D, Kaufmann H (2016) Effects of strain rate on mechanical properties in tension of a commercial aluminium alloy used in armour applications, Procedia Structural Integrity **2**:986-993. DOI 10.1016/j.prostr.2016.06.126

[12] Cadoni E, Dotta M, Forni D, Bianchi S, Kaufmann H (2012) Strain rate effects on mechanical properties in tension of aluminium alloys used in armour applications, EPJ Web of Conferences **26**:05004. DOI 10.1051/epjconf/20122605004

[13] Cadoni E, Dotta M, Forni D, Spaetig P (2011) Strain-rate behavior in tension of the tempered martensitic reduced activation steel Eurofer97, Journal of Nuclear Materials **414**(3):360–366. DOI 10.1016/j.jnucmat.2011.05.002

[14] Cadoni E, Dotta M, Forni D, Tesio N (2011) Dynamic behaviour of reinforcing steel bars in tension, In: Applied Mechanics and Materials (Eds Cadoni E, di Prisco, M) **82**:86–91, Trans Tech Publications Ltd. DOI 10.4028/www.scientific.net/AMM.82.86

[15] Asprone D, Cadoni E, Prota A, Manfredi G (2009) Strain-rate sensitivity of a pultruded E-glass/polyester composite, Journal of Composites for Construction **13**(6):558–564. DOI 10.1061/(ASCE)CC.1943-5614.0000036

[16] Shi Y, Shi J, Luo Z, Liu H, Wang D, Shen H (2020) Experimental investigation on strength and deformation characteristics of red sandstone at strain rates of $10^{-2} \sim 55\ s^{-1}$, Advances in Civil Engineering, Special Issue Advancements in the Analysis and Design of Protective Structures against Extreme Loadings 2020 **2020**:8882976. DOI 10.1155/2020/8882976

[17] Grote DL, Park SW, Zhou M (2001) Dynamic behavior of concrete at high strain rates and pressures: I. experimental characterization, International Journal of Impact Engineering **25**(9):869–886. DOI 10.1016/S0734-743X(01)00020-3

[18] Zhang QB, Zhao J. (2014) Quasi-static and dynamic fracture behaviour of rock materials: phenomena and mechanisms, International Journal of Fracture **189**(1):1–32, 2014. DOI 10.1007/s10704-014-9959-z

[19] Ma L, Li Z, Liu J, Duan L, Wu J (2019) Mechanical properties of coral concrete subjected to uniaxial dynamic compression, Construction and Building Materials **199**:244–255. DOI 10.1016/j.conbuildmat.2018.12.032

[20] Ma L, Wu J, Wang M, Dong L, Wei H (2020) Dynamic compressive properties of dry and saturated coral rocks at high strain rates, Engineering Geology **272**:105615. DOI 10.1016/j.enggeo.2020.105615

[21] Solomos G, Albertini C, Labibes K, Pizzinato V, Viaccoz B (2004) Strain rate effects of nuclear steels in room and higher temperatures, Nuclear Engineering and Design **229**(2-3):139-149. DOI 10.1016/j.nucengdes.2003.10.006

[22] Albertini C, Montagnani M (1977) Dynamic material properties of several steels for fast breeder reactor safety analysis. Final report, EUR 5787 EN, Joint Research Centre Ispra - Applied Mechanics Division.

[23] Nilson M (2003) Constitutive model for Armox 500T and Armox 600T at low and medium strain rates, Swedish defence research agency, Technical report.

[24] Zabotkin K, O'Toole B, Trabia M (2003) Identification of the dynamic tensile properties of metals under moderate strain rates. 16th ASCE Engineering Mechanics Conference, July 16-18, 2003 University of Washington, Seattle.

[25] Kong SY, Remennikov A, Uy B (2010) The effect of medium strain rates on the mechanical properties of high performance steels, 21st Australasian Conference on the Mechanics of Structures and Materials, Melbourne, Victoria, Australia

[26] Cui J, Wang S, Wang S, Li G, Wang P, Liang C (2019) The effects of strain rates on mechanical properties and failure behavior of long glass fiber reinforced thermoplastic composites, Polymers **2019**(11):2019. DOI 10.3390/polym11122019

[27] Mirone G (2013) The dynamic effect of necking in Hopkinson bar tension tests, Mechanics of Materials **58**:84–96. DOI 10.1016/j.mechmat.2012.11.006

[28] Mirone G, Coralloa D, Barbagallo R (2016) Interaction of strain rate and necking on the stress-strain response of uniaxial tension tests by Hopkinson bar, Procedia Structural Integrity **2**:974–985. DOI 10.1016/j.prostr.2016.06.125

[29] Bridgman P (1964) Studies in Large Plastic Flow and Fracture, with Special Emphasis on the Effects of Hydrostatic Pressure, Harvard University Press. DOI 10.4159/harvard.9780674731349

[30] Alves M, Jones N (1999) Influence of hydrostatic stress on failure of axisymmetric notched specimens, Journal of the Mechanics and Physics of Solids **47**:643–667. DOI 10.1016/S0022-5096(98)00060-X

[31] Dietrich L, Miastkowski J, Szczepinski W (1970) Nowość graniczna elementów konstrukcji (Limiting Capacity of the Construction Elements, in Polish), PWN, Warsaw.

[32] Gromada M, Mishuris G, Öchsner A (2011) Correction Formulae for the Stress Distribution in Round Tensile Specimens at Neck Presence, SpringerBriefs in Applied Sciences and Technology, Computational Mechanics, Springer, Berlin, Heidelberg. DOI 10.1007/978-3-642-22134-7

[33] La Rosa G, Mirone G, Risitano A (2003) Postnecking elasto-plastic characterization: degree of approximation in the Bridgman method and properties of the flow-stress/true-stress ratio, Metallurgical and Materials Transactions A **34**(3):615–624. DOI 10.1007/s11661-003-0096-y

[34] Ling Y (2004) Uniaxial true stress–strain after necking, AMP Journal of Technology **5**:37–48.

[35] Malinin NN, Rżysko J (1981) Mechanika materiałów (Mechanics of Materials, in Polish), PWN, Warsaw.

[36] Mirone G (2004) A new model for the elastoplastic characterization and the stress–strain determination on the necking section of a tensile specimen, International Journal of Solids and Structures **41**(13):3545–3564. DOI 10.1016/j.ijsolstr.2004.02.011

[37] Zhang ZL, Hauge M, Odegard J, Thaulow C (1999) Determining material true stress–strain curve from tensile specimens with rectangular cross section, International Journal of Solids and Structures **36**(23):2386–2405. DOI 10.1016/S0020-7683(98)00153-X

[38] Davidenkov NN, Spiridonova NN (1945) Analysis of the stress state in the neck of a stretched specimen (in Russ.), Zavodskaya Laboratoriya (6):583-593.

[39] Mehdikhani M, Aravand M, Sabuncuoglu B, Callens MG, Lomov SV, Gorbatikh L (2016) Full-field strain measurements at the micro-scale in fiber-reinforced composites using digital image correlation, Composite Structures **140**:192–201. DOI 10.1016/j.compstruct.2015.12.020

[40] Jones I, Iadicola ME (Eds) (2018) A Good Practices Guide for Digital Image Correlation, International Digital Image Correlation Society. DOI 10.32720/idics/gpg.ed1/print.format

[41] Li L, Sun L, Dai Z, Xiong Z, Huang B, Zhang Y (2019) Experimental investigation on mechanical properties and failure mechanisms of polymer composite-metal hybrid materials processed by direct injection-molding adhesion method, Journal of Materials Processing Technology **263**:385–395. DOI 10.1016/j.jmatprotec.2018.08.039

[42] Codolini A, Li QM, Wilkinson A (2018) Mechanical characterization of thin injection-moulded polypropylene specimens under large in-plane shear deformations, Polymer Testing **69**:485–489. DOI 10.1016/j.polymertesting.2018.06.010

[43] Röhrig C, Scheer T, Diebels S (2017) Mechanical characterization of a short fiber-reinforced polymer at roomtemperature: Experimental setups evaluated by an optical measurement system, Continuum Mechanics and Thermodynamics **29**:1093–1111. DOI 10.1007/s00161-017-0560-3

[44] McCormick N, Lord J (2010) Digital Image Correlation, Materialstoday **13**(12):52–54. DOI 10.1016/S1369-7021(10)70235-2